

# STIS Coronagraphic Observations of $\beta$ Pictoris<sup>1</sup>

Sara R. Heap, Don J. Lindler<sup>2</sup>, Thierry M. Lanz<sup>3</sup>, Robert H. Cornett<sup>4</sup>, and Ivan Hubeny<sup>5</sup>

*Laboratory for Astronomy & Solar Physics, Code 681, NASA's Goddard Space Flight Center,  
Greenbelt MD 20771*

heap@stis.gsfc.nasa.gov

S.P. Maran

*Space Sciences Directorate, Code 600, NASA's Goddard Space Flight Center, Greenbelt MD 20771*

maran@stis.gsfc.nasa.gov

and

Bruce Woodgate

*Laboratory for Astronomy & Solar Physics, Code 681, NASA's Goddard Space Flight Center,  
Greenbelt MD 20771*

woodgate@stis.gsfc.nasa.gov

lindler@stis.gsfc.nasa.gov

lanz@stis.gsfc.nasa.gov

cornett@stis.gsfc.nasa.gov

hubeny@stis.gsfc.nasa.gov

February 1, 2008

## ABSTRACT

We present new coronagraphic images of  $\beta$  Pictoris obtained with the Space Telescope Imaging Spectrograph (STIS) in September 1997. The high-resolution images

---

<sup>2</sup>Advanced Computer Concepts, Potomac MD 20854

<sup>3</sup>Department of Astronomy, University of Maryland, College Park MD 20742

<sup>4</sup>Raytheon ITSS, 4400 Forbes Blvd., Lanham MD 20706

<sup>5</sup>National Optical Astronomy Observatories, Tucson, AZ 85726, USA

(0".1) clearly detect the circumstellar disk as close as 0".75 to the star, corresponding to a projected radius of 15 AU. The images define the warp in the disk with greater precision and at closer radii to  $\beta$  Pic than do previous observations. They show that the warp can be modelled by the projection of two components: the main disk, and a fainter component, which is inclined to the main component by  $4\text{--}5^\circ$  and which extends only as far as  $\approx 4''$  from the star. We interpret the main component as arising primarily in the outer disk and the tilted component as defining the inner region of the disk.

The observed properties of the warped inner disk are inconsistent with a driving force from stellar radiation. However, warping induced by the gravitational potential of one or more planets is consistent with the data. Using models of planet-warped disks constructed by Larwood and Papaloizou (1997), we derive possible masses of the perturbing object.

*Subject headings:* stars: circumstellar matter, fundamental parameters, individual ( $\beta$  Pictoris), planetary systems

## 1. Introduction

The extensive circumstellar disk of  $\beta$  Pic has been subjected to intense scrutiny and interpretation since it was discovered by Smith and Terrile (1984). These studies have been inspired by the possibility that the  $\beta$  Pic system might be an analogue to the solar system in its early stages or represent a distinct branch of planetary system evolution. In either case,  $\beta$  Pic provides a laboratory in which cosmogonical theories can be tested. Nevertheless, fifteen years after its discovery, the  $\beta$  Pic circumstellar system remains largely a mystery. Is  $\beta$  Pic a proto-planetary environment, in which planets have not yet formed, one where planets already exist, or a “failed” system, where planetesimals, if any, cannot grow further? Spectroscopic indications of cometary bodies (e.g. Vidal-Madjar et al. (1994)) suggest that planet-building has progressed at least to the planetesimal stage, but resolve few issues. These questions are thoroughly reviewed by Artymowicz (1997) from pre-1997 data. Although there is no direct evidence for planets around  $\beta$  Pic, there are intriguing asymmetries in the disk that may be due to gravitational perturbations by substellar objects. The most important of these is a reported  $3^\circ$  tilt of the inner disk ( $r < 50$  AU) with respect to the outer disk (Burrows et al. 1995; Mouillet et al. 1997).

We present new coronagraphic observations made with the Space Telescope Imaging Spectrograph (STIS), as installed on the Hubble Space Telescope in February 1997. The STIS coronagraphs show a greater level of detail, provide higher image quality, and reveal the disk closer in to the

---

<sup>1</sup>Based on observations with the NASA/ESA Hubble Space Telescope, obtained at the Space Telescope Science Institute, which is operated by the Association of Universities for Research in Astronomy, Inc., under NASA contract NAS5-26555

star than prior observations. These observations further characterize the tilt of the inner disk for comparison with theory. In §2, we describe the design and performance of the STIS coronagraph. In §3, we discuss the  $\beta$  Pic observations and data reduction techniques. In §4, we present the observational results. The STIS images show the disk to be warped at close radii to the star in the sense that the inner disk is tilted by 4.6 degrees with respect to the outer disk. In §5, we use the size and shape of the warp to evaluate the two proposed theories of its origin. We conclude that the observations of the warp in the inner disk favors the existence of a planet around  $\beta$  Pic.

## 2. STIS Coronagraphy

Although designed primarily for spectroscopy, STIS easily meets the prime requirements for stellar coronagraphy. It employs an occulting mask and Lyot stop that work together to block out direct and scattered starlight. Because of its high resolution,  $0''.1 = 2$  AU at the Hipparcos distance of  $\beta$  Pic (19.28 pc), it can accommodate small occulting masks, thereby allowing examination of the  $\beta$  Pic disk to within  $0''.5$ , or a projected distance of 10 AU, from the star. Most importantly, its stable point spread function makes possible a definitive separation of the disk’s light from other components. In contrast, WPFC2 lacks a coronagraphic mode; and ground-based coronagraphs, even with adaptive optics, are subject to significant variations in the point-spread function (PSF). Below, we describe the design and performance of the STIS coronagraph.

The STIS design is described by Woodgate et al. (1998), its in-orbit performance by Kimble et al. (1998), and its in-orbit operations by Sahu et al. (1999) in the *STIS Handbook*. Figure 1 shows the optical layout of the STIS coronagraph. Light entering the instrument is corrected for telescope aberrations and for astigmatism at the STIS field point by a two-mirror system similar to that used in COSTAR. After correction, light passes through the coronagraphic aperture mask at the first STIS focal plane. The beam is collimated by an off-axis ellipsoidal mirror and directed to a flat mirror near the second pupil plane, a few millimeters beyond the Lyot stop. The beam then goes to a folding flat and an ellipsoidal camera that focuses the light onto the CCD detector.

Coronagraphic observations on STIS make use of an occulting mask, called 50CORON in the *STIS Handbook*, which is one of 65 apertures that can be inserted into the beam at the focal plane. Its format is clearly seen in Figure 2, which shows a coronagraphic image of HD 60753, a V=6.61 B3III-type star having no known circumstellar structure. The square field is  $51''$  across. The 50CORON aperture mask has a large rectangular bar  $3'' \times 10''$  (top of figure), and two tapered bars (wedges) ranging in width from  $0''.5$  to  $3''$ . For these observations, the star was positioned behind WedgeB1.8, a point where the bar is  $1''.8$  wide.

The halo of the HST PSF is caused largely by light with phase errors from the sagged outer radii of the primary mirror, with some contribution from light diffracted from the edges of the HST primary (Vaughn 1991). A conventional Lyot stop is a baffle at a pupil plane shaped to block light from these sources. The STIS Lyot stop, which is near but not precisely at a pupil plane, is a

circular aperture open to the central 77% of the beam area. It is expected to eliminate error light from both mirror sag and the primary edge. A comparison of theoretical and observational data on  $\beta$  Pic suggests that the Lyot stop decreases the intensity of the PSF halo by a factor of two, but further observations will be needed to quantify the effectiveness of the Lyot stop.

The detector is a back-thinned, UV-enhanced CCD with a  $1024 \times 1024$  -pixel format, each pixel subtending  $0''.0507$ . Hence, one CCD pixel subtends nearly exactly 1 AU at the distance of  $\beta$  Pic. The intra-scene dynamic range of the CCD in a single exposure is 20,600; it can be effectively increased by combining a series of exposures to raise the count statistics while beating down the read noise. The low readout noise ( $1.7 \text{ DN} = 6.8 e^-$ ) and dark current ( $6 e^-/\text{pixel}/\text{hour}$ ) make it possible to probe the  $\beta$  Pic disk out to very low surface brightness.

Since the 50CORON aperture is unfiltered, the UV-enhanced CCD records light over a very wide band, from 2,000 to 10,000 Å. The effective PSF is therefore an average of monochromatic PSFs, each weighted by the stellar flux recorded by the CCD at the corresponding wavelength. The broad response of the detector has the important advantage of blending the diffraction rings, thereby erasing color-dependent structure in the PSF and producing a smooth halo. However, the sensitivity at long wavelengths increases the influence of scattering within the detector. At longer wavelengths, the wings of the PSF are visible out to several hundred pixels from the stellar spectrum.

The coronagraphic image shown in Figure 2 was obtained during the test and evaluation of STIS following its installation on HST in February 1997. Unfortunately, the innermost regions of the PSF are saturated ( $> 144,000e^-$ ). Nevertheless, the deep exposure is useful in revealing structure of the PSF far from the star. The residual starlight outside the occulting bar has unexpected structure. The main features are the small “tuft of hair” that juts out to the upper left from the occulted region and the two long “stool legs” that project downward from the position of the occulted star. The origins of these artifacts are unknown, but they are permanent features of the PSF. Because of this general stability, the PSF can be removed or greatly suppressed from the observations.

In principle, the PSF could be degraded by telescope guidance errors and jitter and by thermal drifts within STIS. In practice, such errors are so small that they can be ignored. However, the telescope is known to experience focus variations (“breathing”) that take place on a timescale of only minutes. Comparison of the three 10-min exposures that comprise the observation of HD 60753 indicates that the effects of such variations are insignificant compared to the intrinsic structure in the PSF. As a demonstration, Figure 3 shows cross-sectional plots of the three exposures. Only in the diffraction spikes can one exposure be distinguished from another. We have found similar stability in our series of exposures of  $\beta$  Pic. Evidently, telescope “breathing” does not noticeably affect the PSF at distances of 1” or more from the star if the exposures are all taken in the same orbit.

### 3. Observations and Reduction

#### 3.1. Observing Strategy and Procedure

Typically, the observing procedure for coronagraphy involves identical observations of the target and a nearby reference star of similar magnitude and spectral type. The intensity-scaled image of the reference star is then subtracted from the target image in order to remove starlight in the target image that was not already blocked by the occulting mask and Lyot stop. This procedure was not followed in our observations of  $\beta$  Pic. Instead, we observed only the  $\beta$  Pic system, but at three different spacecraft roll angles: a roll angle that orients the  $\beta$  Pic disk midway between the telescope diffraction spikes, and at roll angles  $-12^\circ$  and  $+14^\circ$  from the first.

This observing strategy offers two important benefits. The first is reliable detection of structure in the  $\beta$  Pic disk, if present. If an apparent structure remains fixed in images taken at different roll angles, then the feature must be due to the PSF or some detector blemish such as a “hot” pixel; but if the apparent structure rotates with the telescope, then it is identified as originating in the disk. The method of roll separation may not work close to the star if the thickness of the disk is comparable to the linear distance moved between roll angles. In that case, any azimuthally symmetric component of the disk would be rejected and falsely attributed to the PSF. The method of roll separation should be checked by direct subtraction of the PSF as defined by a suitable reference star.

The second advantage of roll separation is suppression of noise induced by the inevitably imperfect determination of the flat field correction. In the reduction, we flat-fielded the  $\beta$  Pic images using an imaging flat of a tungsten lamp. Since  $\beta$  Pic and the tungsten lamp have different spectral flux distributions, the standard flat will have residual errors when applied to  $\beta$  Pic. These residuals are averaged out by observing the disk at different orientations.

Another planning issue is the choice of occulting bar width to be used. The ideal occulting bar is small enough to allow a probe of the  $\beta$  Pic disk close in to the star but large enough that light from the star does not overwhelm the light from the disk nor saturate the detector. We chose to make observations at two spots along the occulting bar: at WedgeB1, which allows a probe to within  $r = 0''.5 = 10$  AU from the star; and at wedge B2, to within  $r = 1'' = 20$  AU.

The observations were taken on 16-17 September 1997 as part of the program of HST early release observations (Program 7125: visits 4-6; rootname=O42V). The observations were so scheduled because in September, the nominal roll of the telescope orients the disk midway between the telescope diffraction spikes. The observing program consisted of three “visits,” each one orbit long, and each at a different spacecraft roll angle. In each visit, the star was first located in the  $6''$  target-acquisition “window” of the CCD. Then the telescope was moved to place the star behind the WedgeB2 occulting bar. Next, a series of 8 five-sec exposures was recorded. Finally, the telescope was repointed to place the star behind the WedgeB1 occulting bar and two sequences of eight 3-sec exposures were taken.

### 3.2. Data Reduction and Solution for the Disk

The data were reduced with the STIS IDT version of CALSTIS (Lindler 1997). In this program, each series of eight exposures was collected into a data-cube, where cosmic ray hits could be identified and removed, and a single average image formed. A bias image appropriate for a CCD gain of 4 was subtracted from the observed image. After conversion to count-rates in  $e^-/\text{s}/\text{pixel}$ , a dark image was subtracted. Hot pixels were identified and removed by reference to a hot-pixel table generated from dark frames made during the week of the observations. The resulting image was flat-fielded with a flat generated from imaging observations of a tungsten lamp. No sky subtraction was performed, since the sky background is very faint. The median pixel value far from the star is  $0.4 e^-/\text{s}/\text{pixel}$  on the WedgeB2 images and  $0.2 e^-/\text{s}/\text{pixel}$  on the WedgeB1 images. In any case, any residual sky light, assumed to be uniform over the field of view, is incorporated in the PSF and removed as part of the solution for the disk.

The diffraction spikes were used to determine the precise location of the star. Although the position of the star was stable during a given visit (telescope roll angle), the position of the star image on the CCD array changed by up to a pixel ( $0''.05$ ) between visits. We therefore geometrically registered the images at the second and third roll angles with the first using the diffraction spikes as fiducials.

A software mask was applied to the diffraction spikes and the edges of the occulting bar in order that they not interfere with the solution for the brightness distribution of the disk. The effect of the software mask, however, is to limit imaging of the disk to distances  $r > 0''.75 = 15 \text{ AU}$  (WedgeB1) and  $r > 1''.24 = 24 \text{ AU}$  (WedgeB2) from the star. Also in preparation for separating the disk and stellar components of each image, a  $512 \times 512$ -pixel region centered on the star was extracted and expanded to  $1024 \times 1024$  pixels.

Separation of the disk and star was achieved in an iterative process. As a starting approximation, the PSF was assumed to be the average of the images from each visit, each at a different orientation. The PSF was then subtracted from each image and the resulting residual images aligned by rotation and averaged to obtain a first estimate of the brightness distribution of the disk. The disk (rotated back to the observed orientation) was then subtracted from each image to get a new estimate of the PSF. This process was repeated 100 times. The solution also involved a rotation of the disk image by  $0.94$  degrees in order to align the disk along a CCD column. Figure 4 shows the results for the WedgeB1 observations.

No reference star was observed, so it was not possible to make a complete check on the roll-separation procedure. Instead, we used the image of HD 60753 (cf Fig. 2), scaled to the brightness of  $\beta \text{ Pic}$ , as a template PSF. Although this star is not a good match in spectral type to  $\beta \text{ Pic}$ , it produces a residual image that is very similar to the disk images obtained by roll separation – except in the region close to the star, where the image of HD 60753 is saturated. Evidently, there is no confusion problem at distances of  $1''.5$  or more from the star.

### 3.3. Evaluation of the Results

Since there are no experimental data available to evaluate the effectiveness of the occulting mask and Lyot stop, we compared the derived PSF for  $\beta$  Pic to theoretical models. Figure 5 compares the radial profile of the derived PSF with that computed from TIM models (Burrows and Hasan 1993). This plot demonstrates the two main advantages of coronagraphy. First, the  $1''$  occulting wedge provides a rejection factor of up to 8000. Were it not for the wedge, the star would produce count-rates of up to nearly a billion  $e^-/\text{s/pix}$ . But because the star is occulted, the dynamic range of the  $\beta$  Pic scene is lowered to a point where it can easily be accommodated by the CCD detector. For example, at  $r = 0''.5$  (10 AU), the occulted star contributes 26,000  $e^-/\text{s/pix}$ , well below the full-well capacity of the CCD (144,000  $e^-$  per pixel) for a 1-sec exposure. Since the readout noise of the summed image (8 or 16 exposures for WedgeB2 and WedgeB1 respectively) is below 1  $e^-/\text{s/pix}$ , its dynamic range is about  $1 \times 10^6$ . Second, the wings of the PSF are a factor of two lower than the TIM model for the telescope performance. This level of suppression accords with the expected action of the Lyot stop, but further observations are needed to complete the characterization of the STIS coronagraphic mode.

Figure 6 compares the radial profiles of light from the star and from the mid-plane of the disk. Not only does the star contribute more light to the disk interior to  $r = 3''$  but also beyond  $9''$ ; this is because the sky background is included in the PSF. Figure 7 shows the disk image with contours of the associated signal-to-noise (S/N) ratios superposed. The errors used to compute the S/N for each pixel were estimated from differences in the six different solutions for the disk (observations at 3 roll angles  $\times$  2 wedge positions). As such, they should represent a total error including both observational uncertainties and errors in the data processing. Along the spine of the disk, the signal-to-noise ratio exceeds 100 over the region from 30 to 150 AU from the star. Above and below the spine of the disk, the brightness and consequently, the S/N, drops rapidly.

## 4. Observed Properties of the $\beta$ Pic Disk

### 4.1. Disk Morphology

Figure 8 (Plate A) shows the resulting images of the  $\beta$  Pic disk based on the WedgeB1 observations. At top is a false-color image of the disk on a log scale. The bottom shows the disk with intensities normalized to midplane brightness, and the vertical scale (i.e. perpendicular to the spine of the disk) expanded by a factor of  $4\times$  in order to show the shape of the disk more clearly. The main visual impressions are the smoothness of the disk and the presence of a warp close (in projection) to the star. The smoothness of the disk in the STIS images is in sharp contrast to previous images (Burrows et al. 1995; Mouillet et al. 1997) which are marked by swirls and radial spikes. We interpret this texture in previous images to incomplete elimination of the PSF. The pronounced warp in the disk was detected in previous images, but only the STIS images are able to

follow it in close to the star. Below, we report on quantitative measurements of the disk, including the radial flux gradient and vertical flux distribution, the warp, and the innermost region of the disk ( $r < 1''.5$ ) that heretofore has not been seen in images of its dust-scattered light. To describe the disk, we use a cylindrical coordinate system with  $r$  denoting the projected distance from the star along the disk midplane, and  $z$  being the distance perpendicular to the disk plane (“vertical” distance).

We measured the radial profile of the disk in three different ways: (*i*) along the midplane defined by the outer disk, averaging over a swath  $\pm 1.25$  AU high; (*ii*) along the curved spine (position of maximum flux), again averaging over a swath  $\pm 1.25$  AU high; and (*iii*) along the midplane, but totalling the flux within a swath  $\pm 100$  AU high. Figure 9 shows the radial brightness profile of the disk along its midplane (method *i*). It shows that the brightness distribution has three segments: an inner region with a rather flat brightness distribution, a transition region, and an outer region where the flux falls off rapidly with increasing radius. We fit the inner ( $r = 1''.6 - 3''.7$ ) and outer ( $r = 6''.7 - 9''.0$ ) segments of the profile by a power law,  $I(r) = r^\gamma$ . Table 1 lists the resulting values of  $\gamma$  for all three methods of measurement.

Table 2 compares our results with previous measurements. In qualitative agreement with others, we find that: the NE and SW sides of the disk are similar at equal radii for  $r < 6''$ ; there is a major change in the brightness gradient at  $r \approx 6'' = 120$  AU; beyond  $r = 120$  AU, the northeast and southwest sides of the disk differ appreciably in brightness and shape. In other respects, the STIS results are quite different from those of previous studies. In the STIS images, the brightness profile of the inner disk is significantly flatter – more in accord with thermal-IR images (Pantin et al. 1997) – and the outer disk much steeper. Thus, the change in slope at  $r \approx 6''$  is much more dramatic in the STIS images ( $\Delta\gamma \approx 4$ ). Evidently, there is a very real change in the density distribution of dust and/or in the scattering properties of the dust at 120 AU from the star.

Figure 10 shows a contour plot of the disk at brightness levels equal to 0.1, 0.5, and 0.99 times the maximum brightness at a given projected radius. The STIS coronagraphic images probe the disk in scattered light closer to the star than previous observations. It is striking that the disk is seen right up to the WedgeB1 (software) mask edge at a projected distance of 15 AU from the star. The WedgeB1 (line) and WedgeB2 (bold) observations agree quite well except at very low surface brightness, where the disk in the WedgeB1 image is more distended vertically than in the WedgeB2 image. We interpret this discrepancy as an indication of uncertainties in the data at low brightness levels. The spine of the disk (99% contours) has an approximately constant thickness but is curved. At half-maximum brightness, the disk shows bulges on either side (Table 3) that are almost round and pinched off smoothly at either end. The full width at 0.1 maximum (FW0.1M) increases with distance from the star consistent with a constant opening angle (wedge shape).

The curvature of the spine of the disk is shown in more detail in Figure 11, which shows both WedgeB1 (line) and WedgeB2 (bold) observations. The two observations give consistent results. The tilt of the inner disk is seen clearly. However, the extensions of the two sides of the inner disk



do not meet at the star. Instead, the spine of the disk dips below the disk equator close to the star ( $r < 1''.5 = 30$  AU). Like Kalas and Jewitt (1995), we interpret this “wing tilt” asymmetry as the consequence of forward-scattering particles in a disk that is inclined to the line of sight. Because of forward scattering, the side of the disk that is closer to the observer will be brighter than the far side. In the case of  $\beta$  Pic, the closer side of the disk is evidently the lower (SE) side. Midway out from the star ( $r = 30 - 120$  AU), the spine is curved. It has its greatest amplitude,  $\Delta z \approx \pm 1.5$  AU, at  $r \approx 70$  AU, somewhat closer in than the bulges revealed by the FWHM contours in Figure 10.

## 4.2. Component structure of the disk

Figure 12 shows the vertical brightness profile at  $r = 90$  AU, where the bulges are most pronounced. The asymmetrical profile suggests the presence of two components: a main component that defines the orientation of the disk, and a fainter component that is offset from the main component. By assuming that each component is symmetric vertically, we were able to separate the two components. The results of the decomposition (Figure 13) indicate that the fainter component is inclined by 4.6 degrees with respect to the main component. The decomposition breaks down close to the star ( $r < 50$  AU) partly because the offset of the inclined component becomes much smaller ( $< 4$  CCD pixels) than the thickness of the disk. Also, errors in the disk structure induced by roll separation of the disk (§3.1) are likely to be significant close to the star. Far from the star, the solution is noisy because of the faintness of the disk.

Figure 14 shows the radial flux distributions of the total disk (both main and tilted components) and tilted components. While the inclined component is detectable at large distances from the star, its brightness beyond  $\approx 80$  AU falls off so rapidly that it is not noticeable in the STIS images, and the measurements are suspect. Inwards of 80 AU, its brightness declines suggesting a central cavity especially on the NE side. At all projected distances from the star, the southwest side of the tilted component is the stronger, whereas the southwest side of the main component (not shown) is somewhat weaker.

The tilted component detected by STIS shows a strong similarity to the inner part of the disk viewed in the thermal-IR at  $12\mu\text{m}$  by Pantin et al. (1997). First, its position angle is  $\text{PA}_{\text{tilt}} = 35.4 = 4.6 + 30.8$  degree (we use the average position angle measured by Kalas and Jewitt (1995) for the position angle of the main component) is the same as the measured position angle of the IR disk,  $\text{PA}_{\text{IR}} = 35.4 \pm 0.6$  degrees Pantin (personal communication). Second, the SW side of the tilted component is brighter than the NE side, as is the case for the IR disk, where the SW side is nearly three times brighter at  $r \approx 3''.6$ . Finally, the tilted component shows evidence of a downturn in brightness at  $r < 2''.5$ , suggestive of a central cavity. Taken by itself, this evidence would be viewed with skepticism in view of potential errors produced in roll separation (§3.1). However, it is consistent with the IR data, which is not vulnerable to such errors.

The overall, multi-wavelength structure of the disk becomes clearer and more intriguing with the recent sub-mm maps of the  $\beta$  Pictoris system reported by Holland et al. (1998). At  $850\mu\text{m}$ , the disk out to  $r \approx 15''$  is an elongated structure whose position angle ( $\text{PA}=32 \pm 4$  degrees) is consistent with the orientation of the main component of the optical disk. However, there is an emission patch further out from the star ( $r = 33''$ ) whose position angle,  $\text{PA}= 37 \pm 6$  degrees, is more in line with the *tilted* component seen by STIS.

Based on these comparisons with IR and sub-mm images, we identify the tilted component as the inner part of the disk seen in the infra-red. We suggest that past interactions in and ejection from the inner disk are responsible for the sub-mm blob much further out. We tentatively identify the main disk component primarily as material further out from the star than  $\approx 80$  AU.

## 5. Interpreting the Warp in the Disk

There are two theories about the origin of the warping of the  $\beta$  Pic disk. In one, the observed warp is formed by the gravitational attraction of a planet in an orbit inclined to the dust disk (Burrows et al. 1995). A similar conclusion was reached by Mouillet et al. (1997), who made numerical simulations to show how the gravitational pull of a major planet in orbit 3-20 AU from the star could warp the disk further out where the bulges are seen. In the other theory developed by Armitage and Pringle (1997), warps naturally form in the inner part of accretion disks surrounding luminous ( $\geq 10L_{\odot}$ ) pre-main sequence stars due to a radiation-induced instability. Both theories predict that the disk will look the same for many thousands of years. The two theories differ, however, in the predicted size and shape of the warp and in their assumptions about the star. With their high image quality and high resolution, the STIS images present stringent observational tests of the models. Below, we compare the STIS observations to predictions of the two theories.

### 5.1. Radiation-Induced Warps

Armitage and Pringle’s simulations follow the development of a radiatively induced warp in  $L \geq 10 L_{\odot}$  stars over the lifetime of the warp (about 20 Myr). In its initial stages, the warp looks like a spiral wave coming out from the star with its greatest amplitude close to the star (see figure 3 of Maloney et al. (1996)) The amplitude of the warp grows to several tens of degrees in a few Myr but then decays on a viscous timescale (a few Myr) when the disk becomes optically thin. Over the course of time, the spiral wave washes out so that the disk looks more symmetrical. According to this theory, the  $\beta$  Pic disk is well into the decay stage.

The inner region of the model disk, while flat and quite thin during the decay phase, is tilted with respect to the outer regions of the disk, but the tilted region only extends out to about 25 AU from the star. If the line of nodes is aligned with the line of sight, the maximum thickness of the disk would occur at  $r = 1''.2$ . Regardless of the angle of the line of nodes, the apparent thickness

should decrease at  $r > 1''.2$ . This is not the case: the observed disk has its maximum vertical thickness in the bulge region at  $r = 4''.5 = 90$  AU.

Another problem for the theory concerns the properties of the star. In order for a radiation-induced warping mechanism to be viable,  $\beta$  Pic must be less than about 20 Myr old, and its luminosity must exceed  $10 L_\odot$ . In interpreting the disk of  $\beta$  Pic, Armitage and Pringle (1997) assumed the stellar parameters derived by Lanz et al. (1995). However, these parameters have been revised because of the new, accurate distance to  $\beta$  Pic from Hipparcos (Crifo et al. 1997), and new, accurate spectrophotometry of  $\beta$  Pic from 3200 to 7350 Å (Alekseva et al. 1996). The new data imply a somewhat lower stellar temperature,  $T_{\text{eff}} = 7950$  K, a lower luminosity,  $L = 8 L_\odot$ , than before, and a minimum age of about 20 Myr.

We conclude that radiation-induced warping is ruled out by observation: the observed warping extends out three times further than predicted; at  $L = 8 L_\odot$ , the star does not have the luminosity needed to induce warping; and at  $\geq 20$  Myr, the system is too old for warping to be detectable.

## 5.2. Warping by a Planet

In the planetary-perturbation theory (Larwood and Papaloizou (1997) and references therein) the shape of the warp depends on the orbital parameters of the planet. For example, if the planet is in an elliptical orbit, one side of the tilted inner disk would extend out further from the star than the other. The radial extent of the warp scales with  $(M_P a^2 t)^{2/7}$ , where  $M_P$  is the mass of the perturber,  $a$  the semimajor axis, and  $t$  the age of the system. The STIS observations showing the disk is warped out to 70 AU or more (Mouillet et al. used 50 AU) require that:

$$\log(M_P/M_\star) + 2 \log a + \log t \approx 6.7$$

where  $a$  is in AU, and  $t$  is in years. Furthermore, we require that  $M_P/M_\star \leq 0.01$ ; otherwise, the perturber would induce stellar radial-velocity variations that are not observed ( $\Delta RV < 1$  km s<sup>-1</sup> according to Lagrange (personal communication)). Table 4 gives some possible values of the mass of the perturber implied by this equation for orbital sizes ranging from 3 AU to 50 AU and for ages ranging from 20 Myr to 100 Myr. It shows that if the  $\beta$  Pic system is young ( $t \approx 20$  Myr) and the companion is very close to the star ( $a < 3$  AU), the warp is produced by a brown dwarf or a very low-mass star. If the perturber is further away (5–50 AU) then the corresponding planetary mass ranges from  $17.4 M_J$  to  $0.17 M_J$ , where  $M_J$  is the mass of Jupiter. If the system is more evolved ( $t \approx 100$  Myr), the same orbital parameters imply a lower planetary mass, down to ten times the mass of the earth.

## 6. Conclusions and Future Work

1. *Coronagraphic performance of STIS.* Observations of  $\beta$  Pic indicate that the STIS coronagraphic aperture and Lyot stop are effective in blocking light from the star. The rejection factor at the PSF core is as high as 8000 even for occulting masks as small as  $1''.0$  in width ( $1''.5$  after the software mask is applied). There is also some suppression of the PSF halo, but further observations will be needed to quantify this performance feature. The PSF has significant structure but is generally stable on a timescale of minutes and days. Because of this stability, the PSF can be substantially removed from the data.

2. *Observed properties of the  $\beta$  Pic disk.* The STIS images clearly define the warp with high precision and at close radii to  $\beta$  Pic. They show that the observed warping of the disk can be resolved into two disks  $5^\circ$  apart. We interpret the brighter component as arising primarily in the outer disk, and the fainter component as arising in the inner region of the disk.

3. *Presence of planet(s) in the  $\beta$  Pic disk?* The observed properties of the tilted inner disk are consistent with the presence of a planet in the disk. Table 5 gives possible masses and orbital sizes of the planet. The STIS observations are consistent with the planetary hypothesis, but before definitive testing of planet-warped models can proceed, they first need to be combined with thermal-emission images in the IR and sub-mm in order to identify the major dynamical processes operating in the disk and to refine the possible parameters of the perturber. One issue to be resolved by the combined observations is the size of the central clearing zone, since that gives an upper limit to the semi-major axis of a planet’s orbit. Another issue is the orbital eccentricity of the perturbing object. An eccentric planetary orbit ( $e > 0.1$ ) has been invoked to explain spectral absorption features formed by “falling evaporating bodies”. The thermal-IR images are ideal in characterizing asymmetries in the inner disk, which could then be used to constrain the eccentricity. We believe that the STIS images described here, when combined IR and sub-mm images should prove useful in constructing a comprehensive model of the disk.

The observations presented here represent a first exploration of the  $\beta$  Pic disk with STIS. Future observations should bring substantial improvement. For example, we can check the present results by observing a suitable reference star and subtracting the image from the  $\beta$  Pic observations to isolate the disk. We plan to follow up the present observations with additional measurements, including coronagraphic spectroscopy.

We thank Merle Reinhart, the program coordinator for program 7125, for accomplishing the challenging scheduling of the  $\beta$  Pic observations. We also thank Chris Burrows, Hashima Hasan, and Mark Clampin for their work in computing the telescope point-spread function. We gratefully acknowledge the advice of Pawel Artymowicz, who suggested that we try decomposing the disk. We also acknowledge the helpful criticisms and suggestions of the anonymous referee. This study was supported by NASA via a grant to the STIS IDT.

## REFERENCES

- Alekseeva, G. A., Arkharov, A. A., Galkin, V. D., et al. 1996, *Baltic Astronomy*, 5, 603
- Armitage P. J. and Pringle J. E. 1997, *ApJ*, 488, L47
- Artymowicz, P. 1997, *Ann. Rev. Earth Planet. Sci.*, 1997, 25, 175
- Artymowicz, P., Burrows C. and Paresce F. 1989, *ApJ*, 337, 494 (ABP)
- Beuzit J. -L., Mouillet D., Lagrange A. -M., and Paufigue J. 1997, *A&A*, (Supplement), 125, 175
- Burrows C., Krist J. E., Stapelfeldt K. R. and WFPC2 Investigation Team 1995, *BAAS*, 187, No. 3205B
- Burrows, C. and Hasan, H. 1993, *The Telescope Imaging Modelling (TIM) Users Manual*, STScI: Baltimore
- Crifo, F., Vidal-Madjar, A., Lallement, R., Ferlet, R., and Gerbald M. 1997, *A&A*, 320, L29
- D’Antona, F. and Mazzitelli, I. 1994, *ApJS*, 90, 467
- ESA 1997, *The Hipparcos Catalogue*, ESA SP-1200
- Ftaclas C., Nonnenmacher, A.L., Gruszcak A. et al. 1994, *Proc. SPIE*, 2198, 1324
- Golimowski D. A., Durrance S.T., and Clampin M. 1993, *ApJ*, 411, L41
- Holland, W.S., Greaves, J.S., Zuckerman, B. et al. 1998, *Nature*, 392, 788
- Holweger, H., Hempel, M., van Thiel, T., and Kaufer, A. 1997, *A&A*, 320, L49
- Kimble, R., Woodgate B., Bowers C. et al. 1998, *ApJ*, 492, L83
- Kalas P. and Jewitt D. 1995, *AJ*, 110, 794
- Lagrange, A.-M., personal communication
- Lanz, T., Heap, S. R., and Hubeny, I. 1995, *ApJ*, 447, L41 (LHH)
- Larwood, John D. and Papaloizou, John C. B. 1997, *MNRAS*, 285, 288L
- Legage P. O., and Pantin E. 1994, *Nature*, 369, 628
- Lindler, D. J. 1997, *CALSTIS Reference Guide*, <http://hires.gsfc.nasa.gov/stis/docs/calstis/calstis.html>
- Maloney, P. R., Begelman, M. C. and Pringle, J. E. 1996, *ApJ*, 442, 582
- Mouillet D., Larwood J.D., Papaloizou J.C.B. and Lagrange A.M. 1997, *MNRAS*, 292, 896

- Pantin E., Lagage P. O., Artymowicz P. 1997, A&A, 327, 1123
- Pantin, E., personal communication
- Sahu, K. et al. 1999, *STIS Instrument Handbook*, STScI: Baltimore
- Schaller, G., Schaerer, D., Meynet, G., and Maeder, A. 1992, A&A(Supplement), 96, 269
- Smith B. A. and Terrile R. J. 1984, Science, 226, 1421
- VandenBerg, D. A. 1985, ApJS, 58, 711
- Vaughn, A. 1991, HIORP report, JPL
- Vidal-Madjar, A., Lagrange-Henri, A.-M., Feldman, P.D., et al. 1994, A&A, 290, 245
- Woodgate, B., Kimble R., Bowers C. et al. 1998, PASP, 110, 1183

Fig. 1.— Optical layout of the STIS coronagraph.

Fig. 2.— Format of a STIS coronagraphic image as shown by an observation of HD 60753 ( $V = 6.61$ ,  $B-V = -0.09$ , spectral type=B3III), a single star having no known circumstellar structure. The field is  $51''$  across. The data were obtained as part of SMOV program 7088 to test the coronagraphic mode of STIS. The image shown here is a raw image, displayed on a logarithmic scale. It is one of three exposures comprising the WedgeB1.8 observation of the star.

Fig. 3.— Stability of the PSF during the observation of HD 60753. Each exposure is identified by a line type as given in the legend. The cross-sectional profiles are taken at line positions,  $l = 324$  (top) through the “tuft of hair” and  $l = 152$  (bottom) through the “stool legs”. The stability of the PSF is such that the three exposures cannot be distinguished from one another. The two bright spikes in either plot are the telescope diffraction spikes.

Fig. 4.— Solutions for the  $\beta$  Pic disk based on WedgeB1 data. The software masks are not applied in these displays in order to show the location of the disk relative to the occulting wedges and telescope diffraction spikes. Each square box is  $512$  pixels =  $26''$  across.

Fig. 5.— Performance of the STIS coronagraph as demonstrated by a comparison of computed (dash-dot) vs. observed PSF’s. The apparent “noisiness” of the predicted profile stems from using only 8 monochromatic PSF’s to represent the PSF for the clear imaging mode. The observed radial flux profiles of the star are shown for WedgeB1 data (line) and WedgeB2 data (bold). Note the large rejection factor at the core of the PSF and the modest suppression of the halo.

Fig. 6.— Radial flux profiles of the spine of the  $\beta$  Pic disk (line) and PSF(dashes). The star is at the origin. Both WedgeB1 (line) and WedgeB2 (bold) profiles are shown.

Fig. 7.— Data quality of the disk image. A greyscale image shows the WedgeB1 observations of the disk on a logarithmic stretch. Contours of  $S/N = 10$  and  $100$  per pixel are overlaid.

Fig. 8.— STIS/CCD coronagraphic images of the  $\beta$  Pic disk (WedgeB2 observations). The half-width of the occulted region is  $0''.75 = 15$  AU. At top is the disk at a logarithmic stretch. At bottom is the disk normalized to the maximum flux, with the vertical scale expanded by 4X.

Fig. 9.— The midplane surface brightness of the  $\beta$  Pic disk (counts/s/pix) as obtained from WedgeB1 observations (line) and WedgeB2 observations (bold line). The NE extension is on top, the SW extension at bottom. The dashed lines show power-law fits to the brightness distribution of the inner region ( $1''.65$ ,  $r$ ,  $3''.67$ ) and outer region ( $6''.7$ ,  $r$ ,  $9''.0$ ). The power-law indices are listed in Table 1 and Table 2.

Fig. 10.— Contour plot of the  $\beta$  Pic disk for both the WedgeB1 observations (line) and WedgeB2 observations (bold line). Three brightness levels are shown: the spine of the disk ( $\geq 99\%$  of the maximum brightness); the full width at half maximum brightness; and contours at  $10\%$  of the maximum brightness.

Fig. 11.— Curvature of the spine of the  $\beta$  Pic disk as indicated by the WedgeB1 observations (line) and WedgeB2 observations (bold).

Fig. 12.— Vertical brightness profiles of the disk at  $r = 90$  AU on the NE side (top) and SW side (bottom). The observed profile is shown in bold, the two components as dashed lines, and the sum of the two components as the line.

Fig. 13.— Vertical offsets of the two components.

Fig. 14.— Radial brightness profile of the observed (line) and tilted (dash-dot) components.



Table 1. Radial Index Measurements

	Northeast Side		Southwest Side	
	Outer	Inner	Inner	Outer
Spine (i)				
WedgeB1	-4.59	-1.25	-1.13	-5.18
WedgeB2	-4.81	-1.32	-1.12	-5.49
Maximum (ii)				
WedgeB1	-4.57	-1.24	-1.05	-5.17
WedgeB2	-4.76	-1.30	-1.02	-5.44
Total (iii)				
WedgeB1	-3.83	-0.89	-0.96	-4.08
WedgeB2	-4.46	-0.95	-0.87	-5.17

Note. — Labels i, ii, and iii refer to methods of measurement described in the text

Table 2. Comparison with Previous Measurements

Region (radius)	Northeast	Southwest	Reference
1.6'' - 3.7''	$-1.28 \pm 0.04$	$-1.12 \pm 0.01$	This paper
2.8'' - 6.0''	$-1.79 \pm 0.01$	$-1.74 \pm 0.04$	This paper
3.0'' - 6.0''	$-1.3$	$-1.3$	MLPL 97
2.8'' - 6.0''	$-2.40 \pm 0.24$	$-2.47 \pm 0.36$	KJ 95
2.4'' - 5.5''	$-2.38 \pm 0.72$	$-1.91 \pm 0.89$	GDC 93
6.7'' - 9.0''	$-4.80 \pm 0.1$	$-5.50 \pm 0.1$	This paper
>6''	$-3.5$	$-3.5$	MLPL 97
6.0'' - 16.0''	$-3.76 \pm 0.05$	$-4.07 \pm 0.05$	KJ 95
6.0'' - 16.0''	$-3.508 \pm 0.0003$	$-4.182 \pm 0.0004$	GDC 93

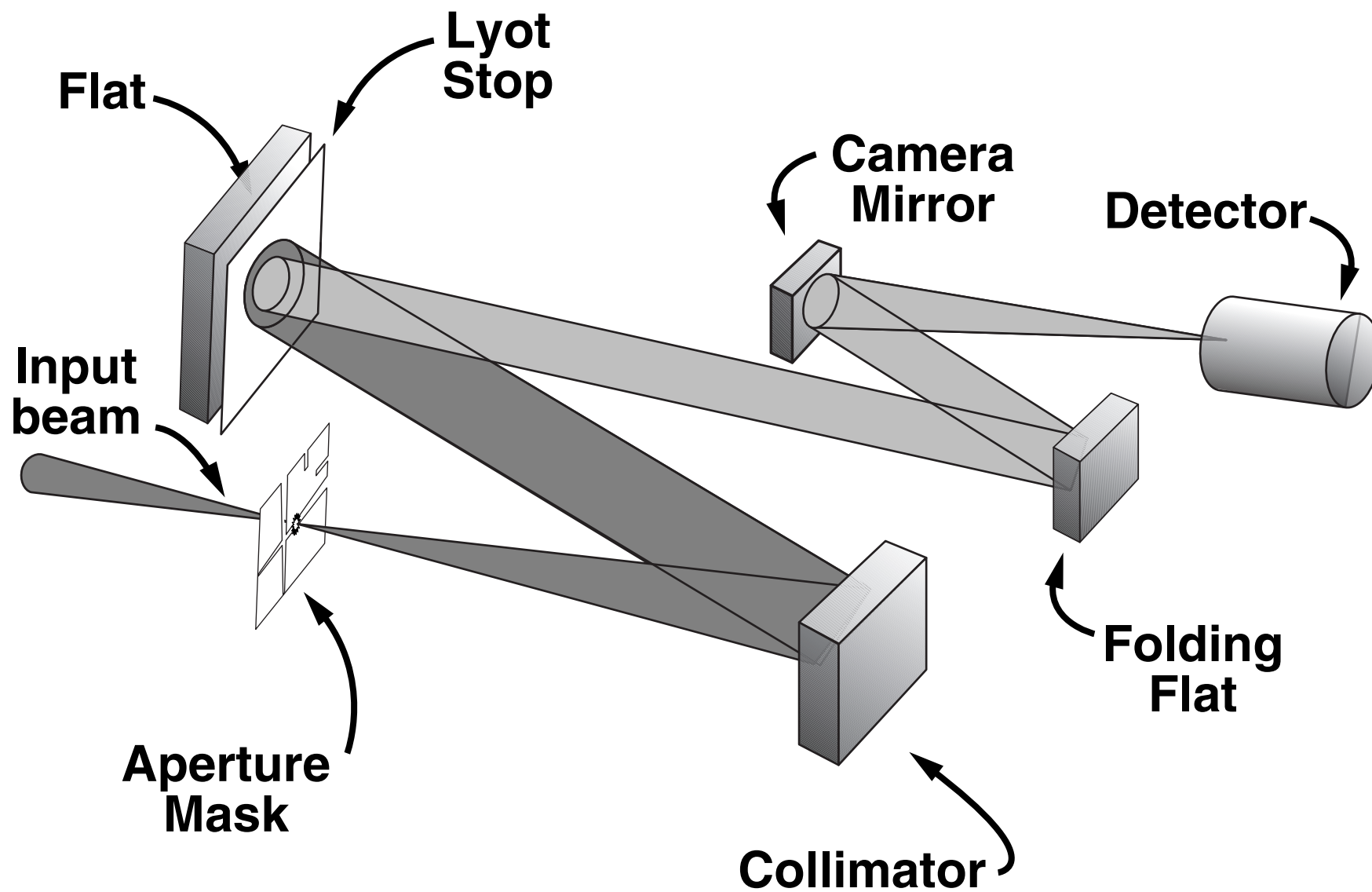
Note. — MLPL 97 = Mouillet et al. (1997), KJ 95 = Kalas and Jewitt (1995), GDC 93 = Golimowski et al. (1993)

Table 3. Thickness of Disk (in AU)

R (AU)	FWHM	FW0.1M
20	17	34
50	16	45
100	18	54
120	15	55
200	22	66

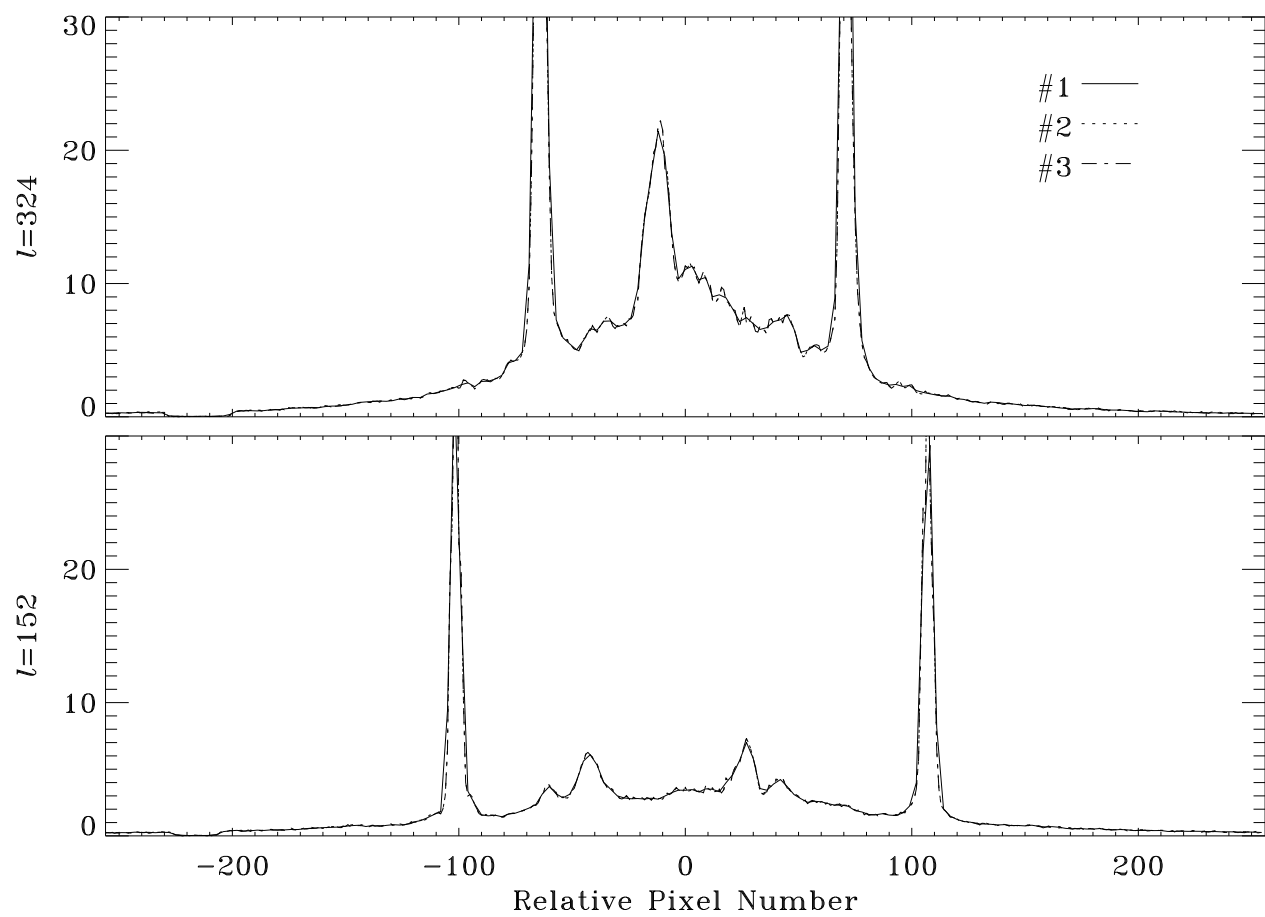
Table 4. Possible Mass of Perturbing Object (in  $M_J$ )

a (AU)	Age (Myr)		
	20	50	100
3	48	19.4	9.7
5	17.4	7.0	3.5
10	4.4	1.7	0.87
15	1.9	0.77	0.39
20	1.09	0.44	0.22
30	0.48	0.19	0.10
50	0.17	0.07	0.035



This figure "figure2.jpeg" is available in "jpeg" format from:

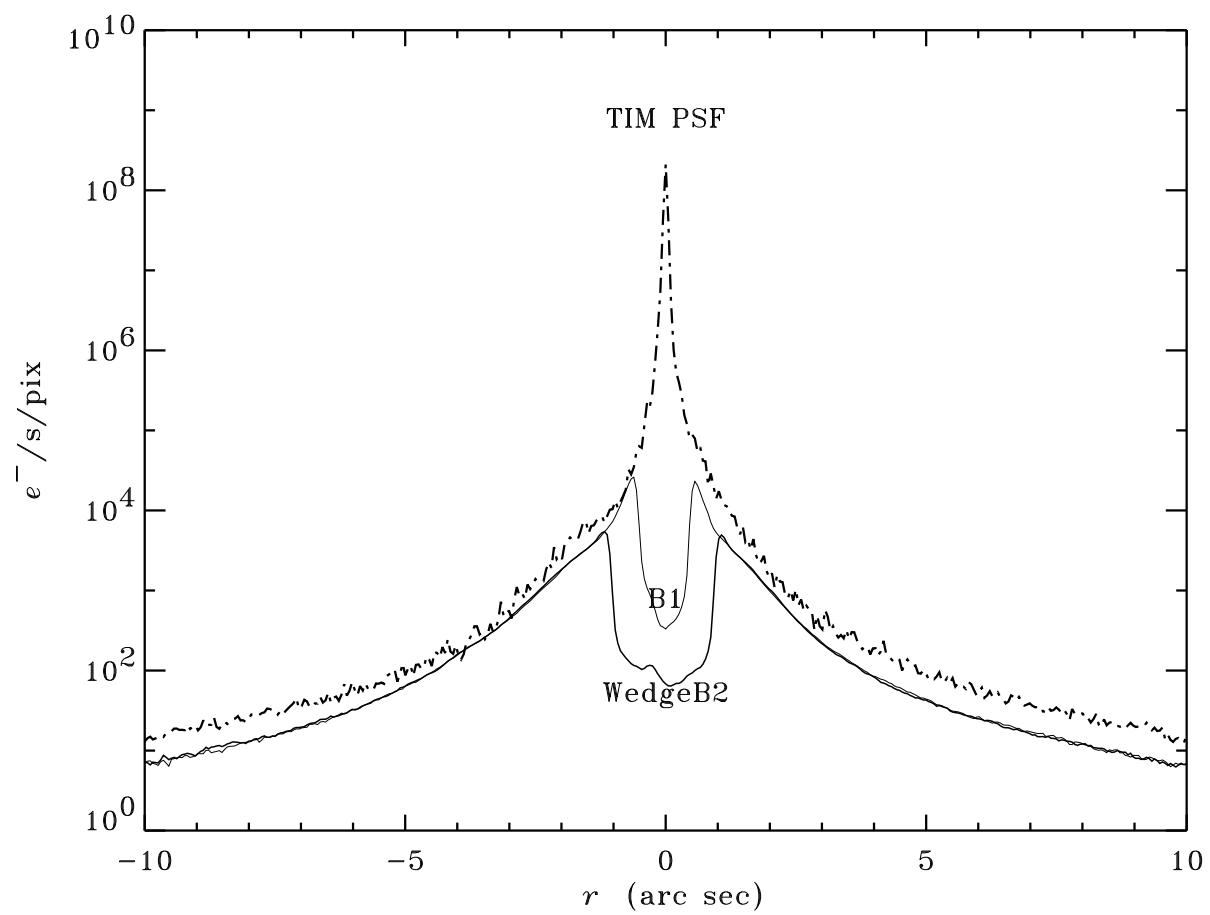
<http://arXiv.org/ps/astro-ph/9911363v1>

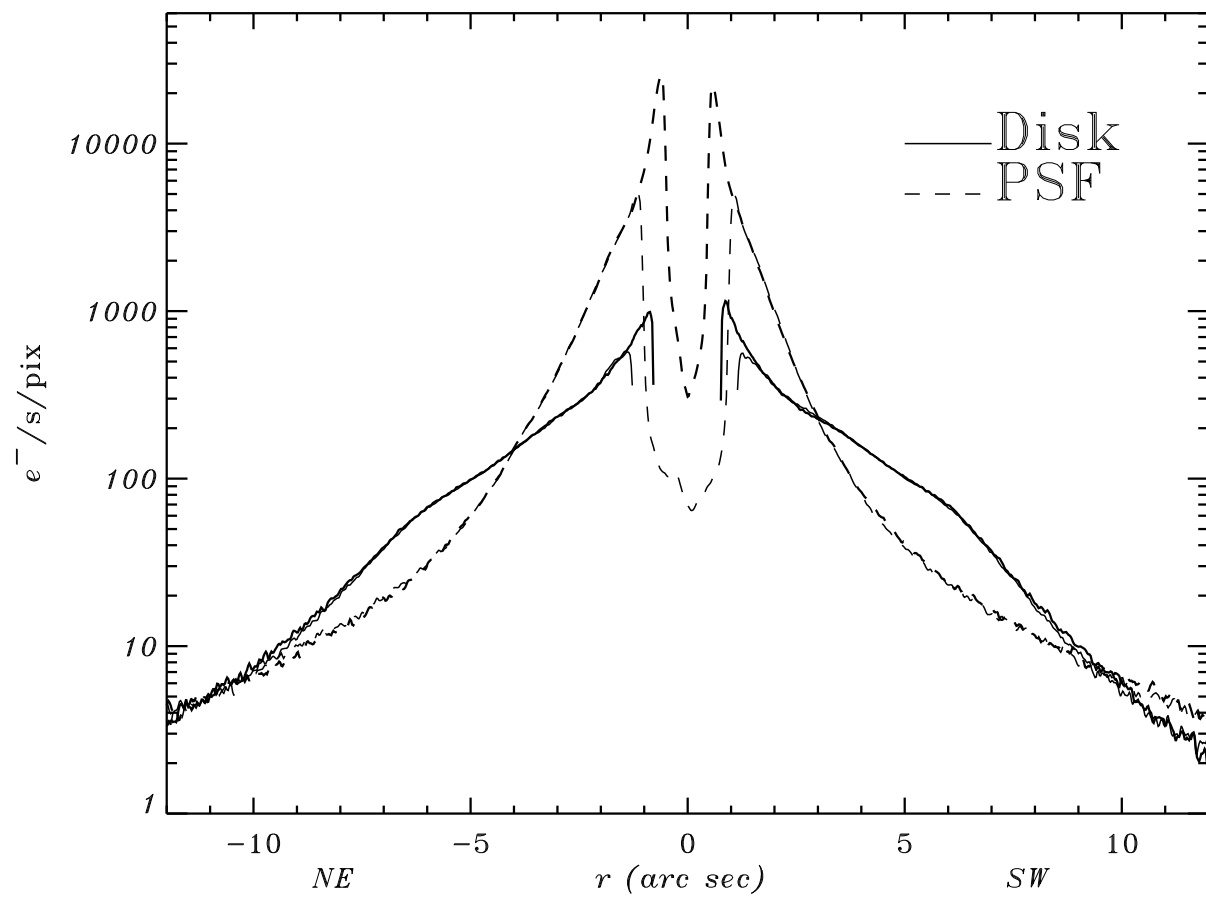


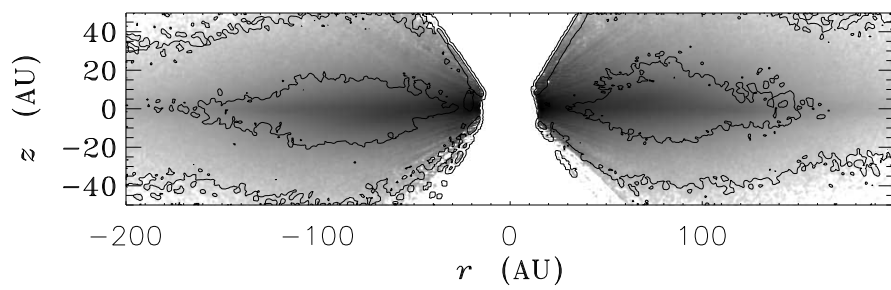
This figure "figure4.jpeg" is available in "jpeg" format from:

<http://arXiv.org/ps/astro-ph/9911363v1>









This figure "figure8.jpeg" is available in "jpeg" format from:

<http://arXiv.org/ps/astro-ph/9911363v1>

